Journal of Environmental and Engineering Geophysics

December 2021
Volume 26
Issue 4
pp. 255–266
DOI: #10.32389/JEEG21-022

Geophysical Reconnaissance for Siting Dryland Critical-Zone Monitoring Experiments in Southern New Mexico, USA

Diane I. Doser[1] and Mark R. Baker[2]

[1]Department of Earth, Environmental and Resource Sciences, University of Texas at El Paso, El Paso, TX 79968-0555, USA
[2]Consultant, 6040 Strahan Road, El Paso, TX 79932, USA

Corresponding author email: bakergrd@cs.com

ABSTRACT

A dryland critical-zone observatory is planned on a piedmont setting of the Jornada Experimental Range northeast of Las Cruces, New Mexico, near a ~10-yr eddy flux covariance tower and vegetation monitoring experiment and a 2-yr old water-uptake rainfall infiltration experiment. We carried out several geophysical surveys to help select sites that minimize geologic complexity for follow up hydrologic and biogeochemical studies that will be conducted by other researchers. First, we conducted a review of regional topography, gravity, and magnetics prior to a site visit and then collected reconnaissance magnetic and electromagnetic data to aid in planning more detailed geophysical site characterization surveys. Our initial topographic analysis using 1/3 arc-second digital elevation models (DEMs) showed the proposed area had an out-of-equilibrium curvature pointing to active erosion and possible faulting. Short-wavelength step-like topographic anomalies in the DEMs were confirmed in LiDAR elevations, and are consistent with erosionally resistant soil horizons in the old alluvial fan deposits. Comparison of 2-D density and susceptibility models based on nearby (3-8 km) hydrostratigraphic studies established that the observed regional gravity and magnetic anomalies were larger than could be modeled with the 2-D structural constraints, and established the station spacing our reconnaissance surveys would require to sample shallow soil variations. Our first site visit confirmed the general fault locations and we identified three outcropping caliche horizons distinct to alluvial channel, proximal splay and distal splay deposits in a several hundred-meter traverse that are consistent with the short-wavelength topographic features. In order to plan additional seismic, radar, gravity, and electrical surveys within a region of such high potential variability, we collected magnetic field and magnetic susceptibility measurements along two profiles at 10-50 m spacing. We found anomalies consistent with two projected faults, as well as other bedrock structures, a result significantly more complex than prior regional hydrostratigraphic mapping had suggested. We also conducted a more limited 0.5 km long ground conductivity survey with 5 m spacing that traversed the rainfall infiltration experiment site and found anomalies that aligned with one of the projected faults. The results showed deep (>6 m) 50 mS/m (milliSiemens/meter) values, indicating moister soils, on the footwall side, dropping to 20 mS/m after crossing the fault, consistent with previous observations that normal faults in the Rio Grande Valley asymmetrically influence fluid flow.

INTRODUCTION

Critical zones (CZ) in dryland regions (aridity index of 0.05 to 0.65, United Nations Convention to Combat Desertification, 2000) are not well studied, although they form a large percentage of Earth's surface (Prăvălie, 2016), and serve as a significant carbon sink (Eswaran *et al.*, 2000; Monger and Martinez-Rios, 2001; Serna-Perez *et al.*, 2006; Zamainan *et al.*, 2016). Researchers at the University of Texas at El Paso are examining the role that dryland CZs play in Earth systems and quantifying the impact of climate variability on carbon storage at three CZ sites within the Rio Grande rift region of southern New Mexico and west Texas (Fig. 1). In this paper we specifically focus on initial geophysical characterization of the Piedmont CZ site on the Jornada Experimental Range (JER) (Fig. 1) to aid in selecting sites for detailed hydrological and soil investigations by other researchers.

The Piedmont CZ site (Fig. 1) lies on a gently west-sloping fan surface approximately 7 km from the crest of the San Andres Mountains and 10 km from the flatter, depositional center of the Jornada del Muerto basin. The general locality was selected based on its proximity to an eddy flux covariance tower and vegetation monitoring experiment that has been operating for over 10 yr and 2-yr-old water-uptake/rainfall infiltration experiment. The researchers conducting the hydrogeologic, drilling, soil sampling and geochemical CZ studies preferred to locate their investigations in a subregion that would be most compatible with 1-D hydrologic model conditions.

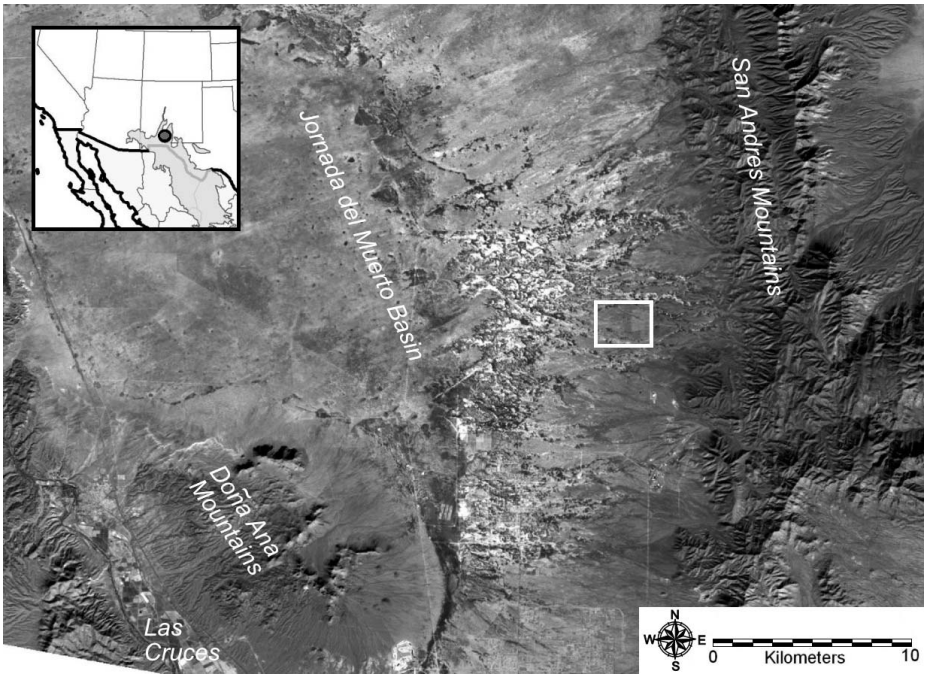

Figure 1 Location of Jornada del Muerto study area and Piedmont site (box). Inset map shows location of Chihuahua Desert (gray region) with dot indicating the Jornada del Muerto study area (after Browning *et al.*, 2011).

A variety of geophysical techniques, including seismic, resistivity and ground penetrating radar, have been used successfully at other CZ sites to image depth to bedrock, determine the role of faulting and fracturing in water transport, and map groundwater flow after a CZ site had been established (*e.g.,* St. Clair *et al.*, 2015; Olyphant *et al.*, 2016; Flinchum *et al.*, 2018; Novitsky *et al.*, 2018). Our study differs from these by using geophysics as a rapid method to help initially select a CZ site that minimizes model complexity. Lessons learned at the Piedmont site will aid in the selection of a second CZ site within a structurally complex playa on the JER and a third CZ site within a flood irrigated agricultural field located on soils derived from fluvial deposits of the Rio Grande within southeastern El Paso County, Texas.

DATA AND METHODS

Previous Studies

The Piedmont CZ site lies at the eastern edge of the Jornada del Muerto basin adjacent to the western San Andres Mountains composed of Paleozoic carbonates, gypsum, sandstones and shales (Hawley and Kennedy, 2004; Fig. 2). Tertiary volcanics outcrop to the southwest and southeast of the site (Fig. 2) and water wells intersect volcanic intrusions (Maciejewski and Miller, 1998) throughout the southern portion of the basin. Hawley and Kennedy (2004) indicate several normal faults related to Cenozoic extension of the Rio Grande rift lie 6–7 km south-southeast of the Piedmont site (dashed black lines, Fig. 2).

Groundwater recharge within the Jornada del Muerto basin occurs primarily from the San Andres Mountains (Hawley and Kennedy, 2004). Most groundwater remains isolated within the basin, although there appears to be minor underflow at the southwest and northwest edges of the basin (Hawley and Kennedy, 2004).

Maciejewski and Miller (1998) conducted a detailed geophysical study as part of an environmental cleanup assessment at a NASA facility located ~8 km south of Piedmont site (Fig. 2) using a combination of 95 gravity readings, 100 water wells, and a re-interpretation of 67 km of seismic lines to image local faults and the depth to water table. They encountered two major NNW-SSE trending, high angle (65–75° dip) normal fault systems at the site, along with a series of minor faults that stair-step into the basin (bold lines, Fig. 2).

The eastern fault system, including the Hardscrabble Hills fault (HHF) and Western Boundary fault zone-2 (WBFZ-2), separates the mountain pediment covered with 0 to 10 m of alluvium from a transitional region of faulted bedrock that dips 3° to the west and is covered by alluvium varying between 100 and 230 m in thickness (Maciejewski and Miller, 1998). The HHF separates Tertiary volcanic units on the west from the Paleozoic section on the east, with no apparent offset of the bedrock surface (Maciejewski and Miller, 1998). Maciejewski and Miller (1998) speculate that the WBFZ-2 may represent either a

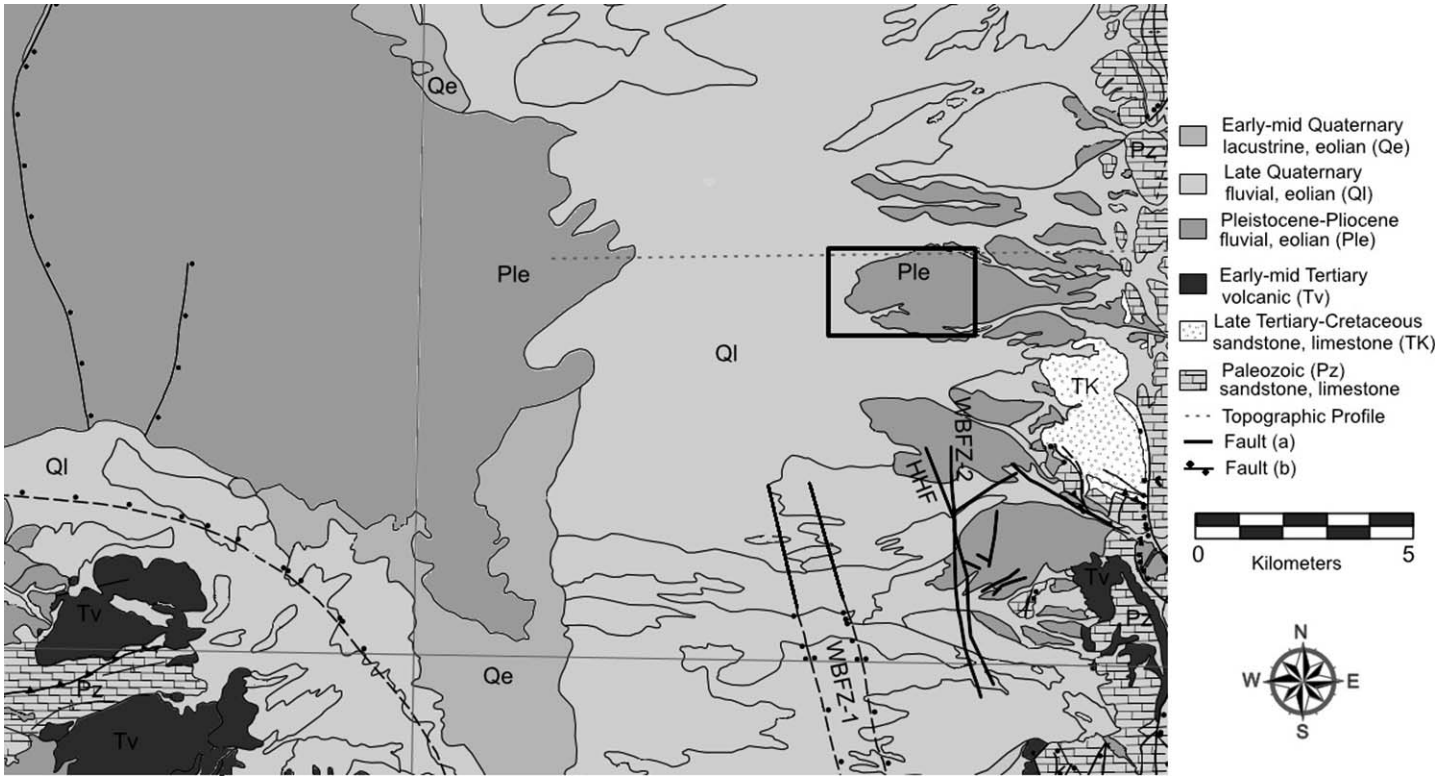

Figure 2 Simplified geology of Piedmont site (box) and surrounding regions. Shading, patterns and abbreviations correspond to legend at right. Map after Hawley and Kennedy (2004). Bold lines (labeled (a) in legend) are faults from Maciejewski and Miller (1998). Other faults (labeled (b) in legend) are from Hawley and Kennedy (2004). Thin dotted line at northern edge of study area shows location of topographic profile shown in Fig. 3. In this and subsequent figures HHF is the Hardscrabble Hills fault. WBFZ-1 and WBRZ-2 are the Western Boundary fault zones 1 and 2, respectively.

separate, younger fault, or a splay of the HHF. Based on gravity modeling they estimate a vertical displacement of 1950 m across the eastern fault system. The western fault system, including the Western Boundary fault zone-1 (WBFZ-1), is the major basin bounding structure that separates the transition region from the Jornada del Muerto basin (Fig. 2). West of the WBFZ-1 alluvium exceeds 600 m in thickness (Maciejewski and Miller, 1998).

In addition to these major faults, the region of the NASA facility is cut by a series of smaller NE-SE trending faults having vertical offsets of 12–30 m that may accommodate left-lateral strike-slip motion (Maciejewski and Miller, 1998). Water well information indicates ground water flow at the NASA facility occurs through both alluvium and two paleochannels within the bedrock (Maciejewski, 1996). Several buried volcanic units (flow banded rhyolite and porphyritic latite) appear to impede ground water flow (Maciejewski and Miller, 1998).

Existing Data Sets

In order to determine if the faults observed south of the Piedmont site continue northward and have topographic expressions across the site, we analyzed digital elevation models (DEM) and LiDAR. We extracted these data from the United States Geological Survey (2021) geospatial database for the eastern JER. The DEM were provided at 1/3 arc second (~10 m grid) and LiDAR at ~1 m grid.

Besides examining changes in topographic profiles extracted from the DEM and their relation to the location of suspected faults (Fig. 3), we analyzed shorter wavelength, near surface features by high pass filtering the DEM and LiDAR data. We accomplished this by subtracting a smoothed, average topographic map (obtained by applying a low pass filter to the topography) from the original DEM and LiDAR data (Fig. 4).

We obtained regional aeromagnetic and gravity data (Fig. 5) from a North American database originally compiled by the Pan-American Center for Earth and Environmental Studies at the University of Texas at El Paso. Regional gravity data (Fig. 5) are sparse. We also suspect the flight lines for the aeromagnetic data were oriented north-south, making it difficult to locate north-south trending features, such as basement faults.

We used geologic constraints from Hawley and Kennedy (2004) and Maciejewski and Miller (1998) to develop a 2-D model of basement structure across the Piedmont site (Fig. 6). The model was then modified to better match the observed regional aeromagnetic

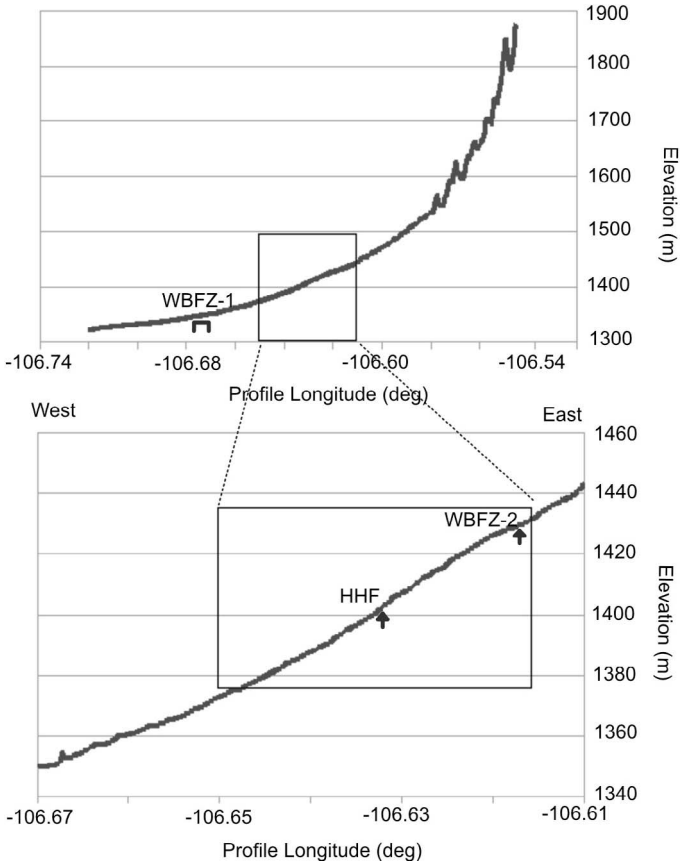

Figure 3 (top) Topographic profile from the San Andres Mountains to the Jornada del Muerto Basin (see Fig. 2 for location of the profile). The box indicates the Piedmont study area. (bottom) Topographic profile across the northern edge of the Piedmont site. Arrows indicate where faults mapped by Maciejewski and Miller (1998) are projected to intersect the profile.

and free-air gravity data using a modified version of the modeling technique of Khatun *et al.* (2007). The use of free-air gravity data requires us to directly compute contributions of surficial geology and topography, and the structural variations above sea level, in our 2-D models (Fig. 6). The regional geophysics are inconsistent with the 2-D model based on expected geology, pointing to the need for a more complex geologic model.

We first visited the Piedmont site in October 2020 to determine where it would be possible to conduct geophysical studies and to discuss other researchers' planned experiments. We noted topographic, soil and vegetation changes that might be linked to deeper structures such as fault zones, as well as evidence for shorter wavelength features that might be visible in the filtered DEM and LiDAR data.

Geophysical Reconnaissance Studies

Following our initial visit in October, we conducted three one-day long reconnaissance trips to the site (Fig. 7). Our first field day (December 2020) involved the collection of ground magnetic data along a road and fence line bordering the north side of the site for rapid evaluation of the depth to basement. We also collected ground conductivity data to evaluate its relation to grain size variations and the presence of pedogenic carbonates observed across the site. Our second field day in February 2021 focused on improved imaging of major basement features through the collection of additional magnetometer data to the south and west of our original line (Fig. 7). We also collected magnetic susceptibility data during the second and third field day (also in February 2021) to determine the variation in the magnetic properties of surface materials.

We used a proton precession magnetometer for our magnetic surveys (large dots, Fig. 7). Spacing along the magnetic profiles varied from 50 m, when walking away from our magnetic base, to 10 m when walking back toward the base to better define regions where we had initially observed large variations in magnetic readings. We corrected the magnetic data for diurnal drift effects. We collected the magnetic susceptibility readings using a KT10 magnetic susceptibility meter with a nominal spacing of 50 m (small dots, Fig. 7) along the same lines as the magnetic surveys.

We used an EM31 ground conductivity meter to collect conductivity measurements (operating the meter in both vertical and horizontal loop modes) along a 550 m long line at ~5 m intervals (diamonds, Fig. 7). We converted these measurements to ground conductivity using the equations given in McNeill (1980).

RESULTS

Regional DEM and LiDAR Data

We extracted a topographic profile from the DEM extending from the crest of the San Andres Mountains to the basin (Fig. 3, top) across the Piedmont site (box). The profile shows a major change in surface slope across the site (arrow) that may represent the extension of WBFZ-2 (Fig. 2). Enlarging the topographic profile to the boundaries of the site itself (Fig. 3, bottom) reveals a series of stair step-like features. Arrows indicate changes in topography that may be associated with the extensions of the WBFZ-2 and HHF.

The stair step patterns in topography became more apparent when we produced a high pass filtered map of the DEM (Fig. 4(a)). We adjusted the map colors in Fig. 4(a) so that above average topography appears in red and below average in blue, with colors saturating at 0.7 m above and below the average, respectively. The map suggests northwest-southeast trending ridges and valleys with stair step changes in

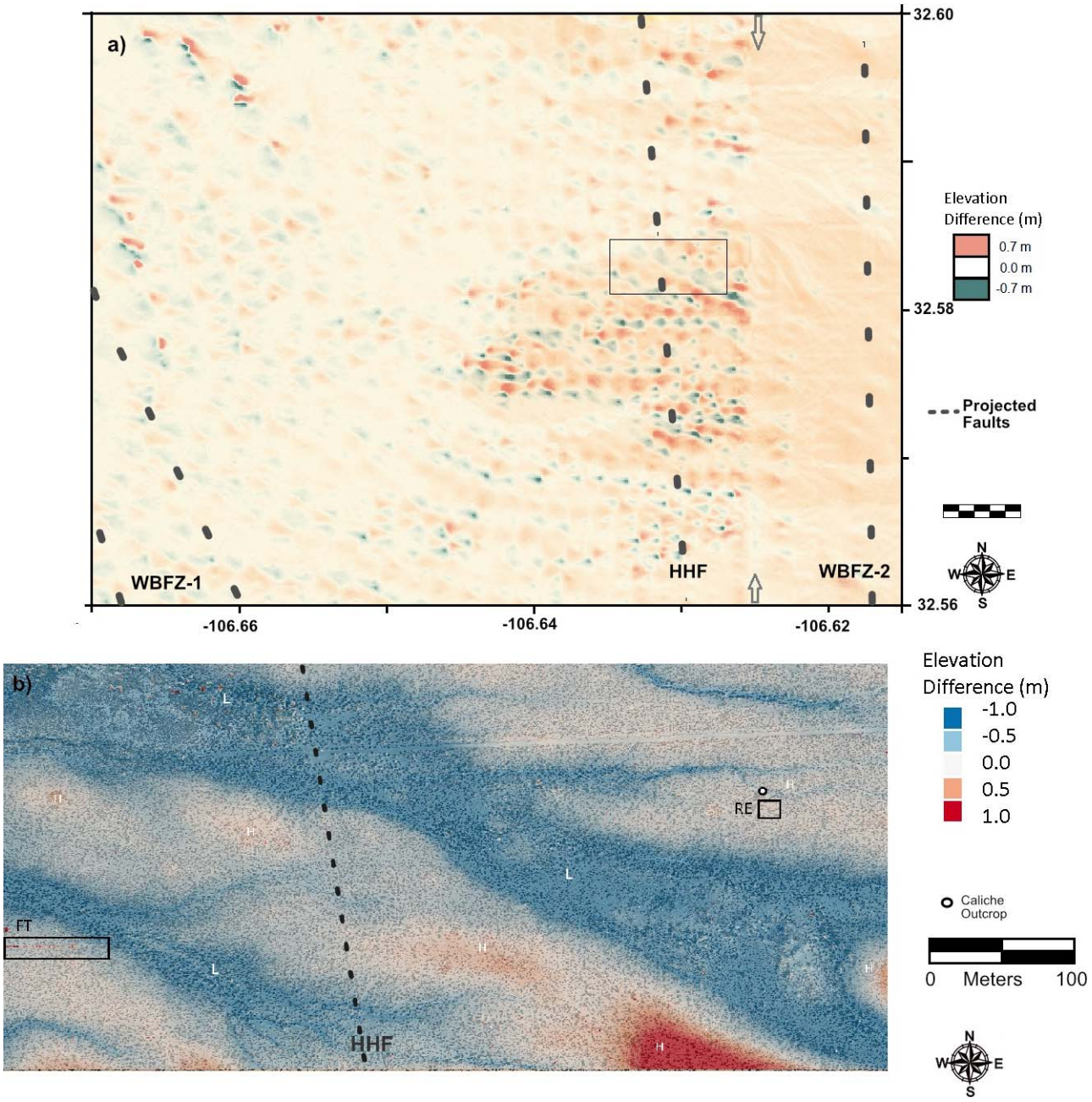

Figure 4 (a) High pass filtered DEM map of the Piedmont site. Arrows indicate the location of an artifact in the DEM data caused by a splice between two DEM sources; and (b) High pass filtered LiDAR data. L indicates region with below average elevation and H indicates region with above average elevation. FT is the location of the eddy covariance flux tower and RE is the rainfall experiment site. The dot indicates a pedogenic carbonate located 10 m north of a soil test pit. The dashed line is the projected location of the HHF.

elevation along both the ridges and valleys. We were concerned that these apparent stair step features could be an artifact of the data set, given one clearly visible artifact in the map located between −106.62 and −106.63 longitude (arrows, Fig. 4(a)) that appears related to the joining of two different topographic data sets. Therefore, we used the high pass filtered LiDAR data to verify our DEM results.

Figure 4(b) shows the high pass filtered LiDAR map of the northern section of the Piedmont study area (location shown in Fig. 4(a) as a rectangle). The LiDAR map confirms the northwest-southeast trending ridges and valleys, with stair step-like features appearing within the ridges and valleys, similar to what we observed in the DEM map. This pattern is especially visible along the topographic high located in the center of Fig. 4(b).

Analysis of Existing Gravity and Magnetic Data

Sparse free-air gravity data (dots, Fig. 5) indicate a consistent decrease in values (dark grays) between the projected locations of the WBFZ-2 and HHF with a corresponding increase in the magnetic field (contour

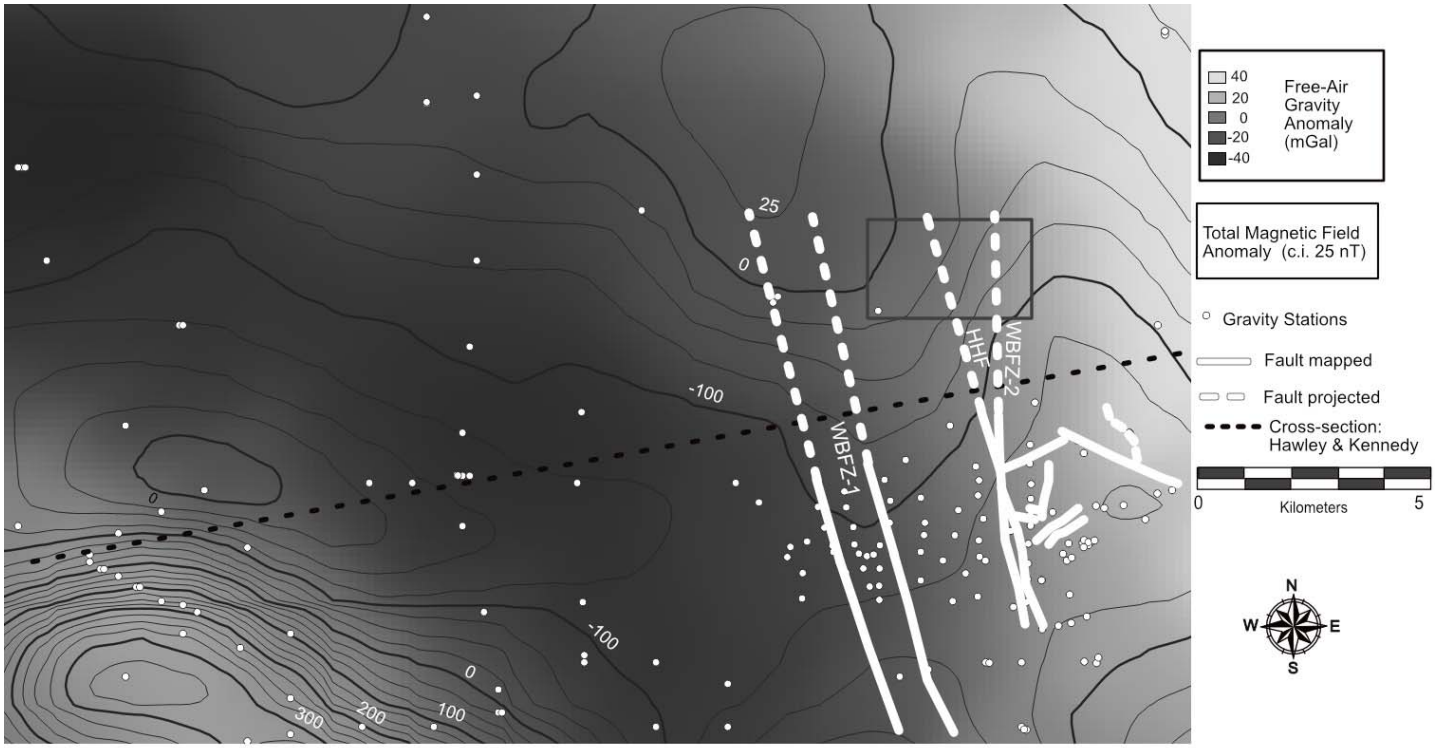

Figure 5 Regional free-air gravity and total magnetic field anomaly data for the Jornada area. Box indicates Piedmont site. Contours indicate magnetic field anomaly (25 nT contour interval) and shading indicates free-air gravity anomaly. Dots indicate gravity observations. Dashed black line is the location of Hawley and Kennedy's (2004) cross section B-B′.

lines). West of the HHF, both the free-air gravity anomaly and total magnetic field appear to level off. The magnetic field and free-air gravity anomaly highs in the southwestern corner of Fig. 5 are related to volcanic rocks of the Doña Ana Mountains (Figs. 1–2).

We developed a preliminary geologic cross section (Fig. 6) across the northern Piedmont site by extracting surface geology (Hawley and Kennedy, 2004), and topography, projecting faults mapped to the south (Hawley and Kennedy, 2004; Maciejewski and Miller, 1998) that were also supported by the observed topographic variations (Fig. 3) and thickness/fault information from the hydrostratigraphic cross section B-B' of Hawley and Kennedy (2004) located ~3 km south of our profile (see Fig. 5). We then adjusted our model bodies using density and magnetic susceptibility values given in Table 1 so that the predicted data (bold lines) more closely approached the observed, interpolated data (x's, Fig. 6). A reasonable match of the observed and predicted data was impossible, indicating the need for a more complex geologic model.

Since the free-air gravity anomaly data were extremely sparse (Fig. 5), we concentrated on matching the observed total magnetic field data (top, Fig. 6). In order for us to obtain a better match to the observed magnetic field changes; we needed to extend the Tertiary volcanics (Tv, Fig. 6) farther to the east than in the cross section of Hawley and Kennedy (2004). Note, however, that magnetic data (Fig. 5) indicate lower total magnetic field values south of the Piedmont site near Hawley and Kennedy's profile. The dashed line in the top model (Fig. 6) indicates the predicted magnetic field at an elevation of 300 m above the surface. The solid line is the magnetic field predicted at 2 m above the surface (the height of the magnetometer sensor), suggesting we should observe a change of at least 5 nT as we crossed the HHF. The response of the potential fields to geologic variations points to needing a 50m magnetic field sampling interval to capture regional characteristics, while a 10–20 m spacing would be needed for shallow variations.

Site Observations

The most significant topographic, sedimentologic and vegetation changes we observed at the northern edge of the site occurred in the region where we had projected the HHF should be located based on our topography and magnetic/gravity modeling. The high-pass LiDAR map indicates this suspected fault appears to deflect a major arroyo system (Fig. 4(b)). The high-pass DEM data (Fig. 4(a)), however, do not appear to show any features related to projections of the HHF, WBFZ-1 or WBFZ-2.

In regions where the DEM and LiDAR analysis indicated below average topography (Figs. 4(a)–(b))

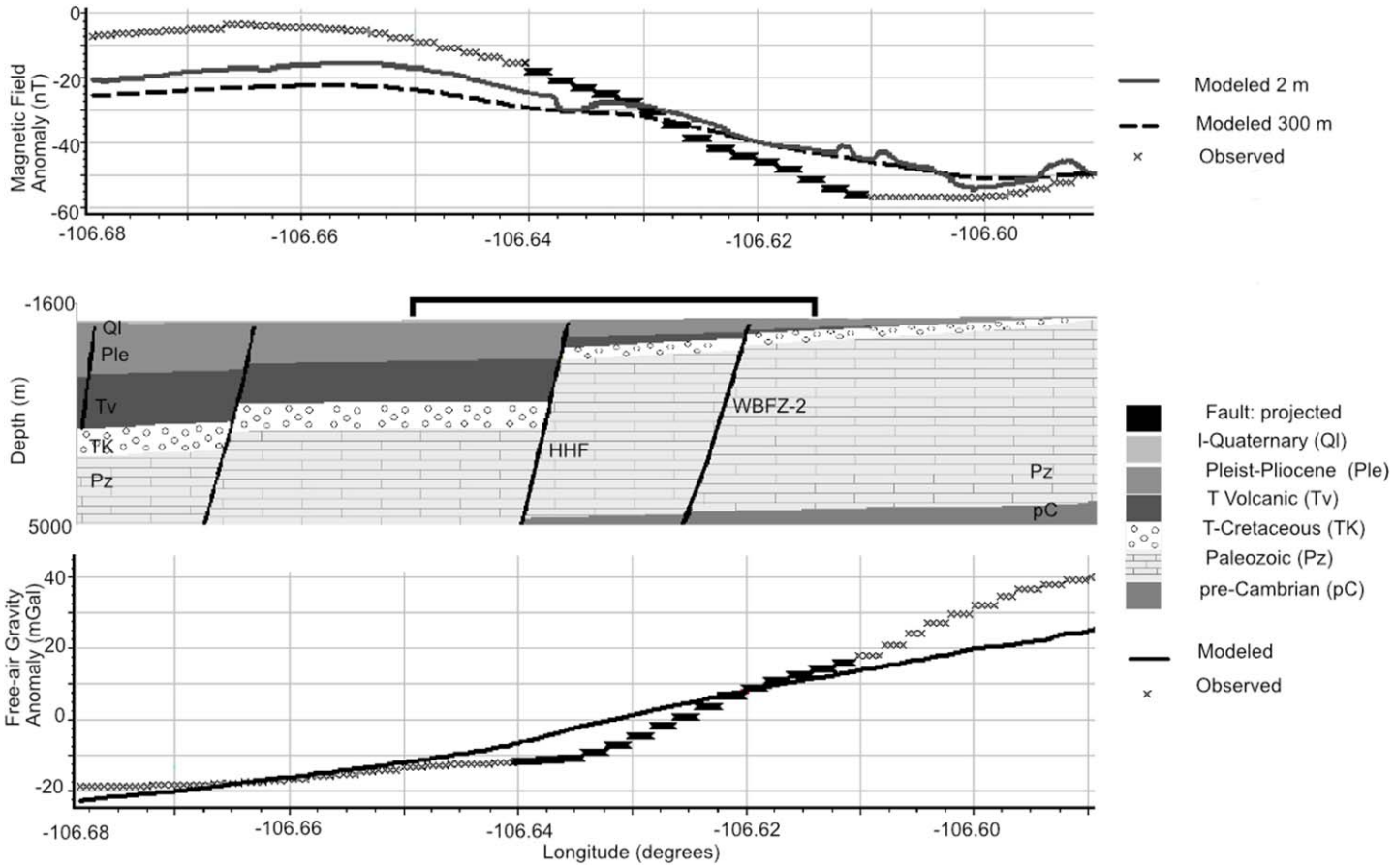

Figure 6 Geological cross section across the Piedmont area (bracket) compared to magnetic field anomaly (top) and free-air gravity anomaly (bottom). X's are observed interpolated data, lines are predicted data based on the geologic model (see legend at fight for abbreviations of geologic units). Table 1 gives the density and magnetic susceptibility values for the geologic units used in the model. The dashed line shows the predicted variation in magnetic field anomaly at a height of 2 m above the surface, the height of our sensor for ground based measurements.

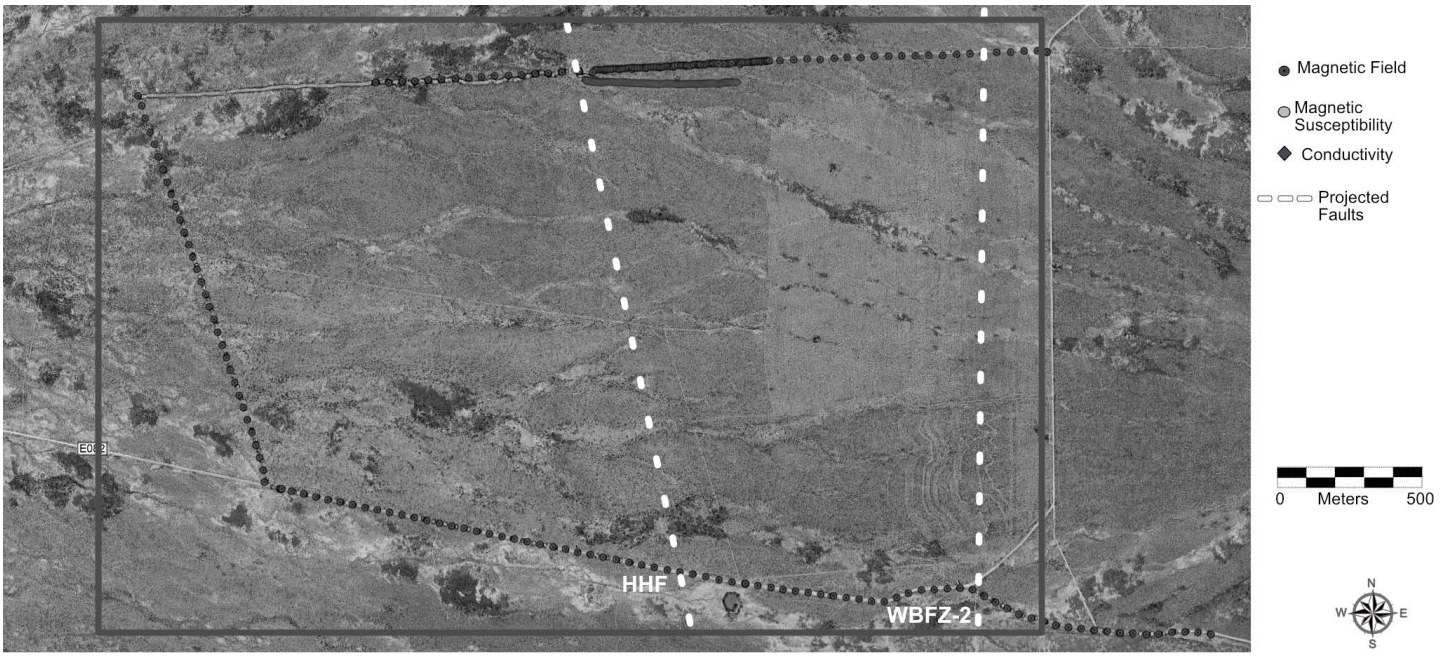

Figure 7 Satellite image showing locations of reconnaissance geophysical surveys (magnetics, magnetic susceptibility, conductivity). Box denotes the entire Piedmont study area.

Table 1 Densities and magnetic susceptibilities used in modeling regional data.

Unit	Abbreviation	Density (kg/m^3)	Magnetic susceptibility (1×10^{-3} SI)
Fault		2480	0.50
Late Quaternary basin fill	(Ql)	2220	0.38
Pleistocene-Pliocene fluvial, eolian	(Ple)	2240	0.8
Tertiary volcanic	(Tv)	2790	10.2
Tertiary-Cretaceous marine sediments	(TK)	2520	0.55
Paleozoic undifferentiated	(Pz)	2620	0.3
Pre-Cambrian undifferentiated	(pC)	2750	0.8

we observed a pebble-rich surface containing little fine grained material, including the region surrounding the eddy flux covariance tower (FT, Fig. 4(b)). In regions of above average topography, we observed discontinuous pedogenic carbonates outcropping at different elevations as well as regions of fine-grained sediments. The carbonates appeared to be forming in alluvial fan channels as well as proximal and distal crevasse splay deposits. A shallow soil test pit (~0.7 m deep) dug in fine grained surface material located less than 10 m south of an outcrop of pedogenic carbonate (dot, Fig. 4(b)) developed in a fan channel deposit, showed little evidence for layering or grain size variation, confirming the discontinuous nature of the pedogenic carbonates.

Magnetic Field and Susceptibility Data

Our magnetics data show large changes in magnetic field across the study area (Fig. 8). There is a variation of >500 nT along the north line and >600 nT along the south line. The west line shows a variation of <110 nT. We observe four features common to the east-west trending north and south lines (Fig. 8). Feature A is the largest peak observed on both profiles, B is a smaller peak located near the middle of profiles, C is the region of the lowest readings (appearing broader on the north line) and D is a peak at east end of the profiles. The satellite image shown on the bottom of Fig. 8 indicates how these four features appear to cut across the study area compared to the projected trends of the HHF and WBFZ-2, and diverge from the trend of outcrops of Cretaceous/Paleozoic deposits to the east in the San Andres Mountains.

We sampled magnetic susceptibility every 50 m along the south and west lines, but every 10 m along the north line (Fig. 8). Two of the lows ($<1 \times 10^{-3}$ SI) (inverted triangles, Fig. 8) correspond to outcrops of pedogenic carbonates while several other lows (triangles, Fig. 8) are associated with heavily vegetated regions. Highs over 2×10^{-3} SI did not correlate with any noted surface features. In areas of desert pavement, the surficial aggregate susceptibility was low ($<1 \times 10^{-3}$ SI), although we found that the sediments located 5-10 cm below the surface aggregate had higher susceptibilities ($>2.5 \times 10^{-3}$ SI).

Ground Conductivity Data

The interpreted shallow and deep conductivities from the EM-31 survey are illustrated in Fig. 9, along with the coincident elevation deviation from the LiDAR data, and the detrended magnetic field derived from measurements we took less than 75m north of the conductivity line (see Fig. 7). The elevation shows three steps that correspond directly to the shallow conductivity structure. The flat steps show lower shallow conductivities than the transitions between steps that correspond to higher conductivities. The deep conductivity estimate shows a region of lower conductivity under the western step. The transition between elevation steps generally correlates to the high gradient regions in the magnetic field.

The lowest values of shallow and deep conductivities occur under the western step and are directly adjacent to the highest conductivities under the middle step. This conductivity change requires a significant lateral change in moisture content in the soils. This area is east of the HHF projection (Fig. 7), but coincides with the anomalous concave downward curvature seen in the topography. The eastern half of the profile with low conductivity and consistent slope corresponds with pedogenic carbonate deposits observed in small drainage channels. At the finest scale, it is clear from the conductivity noise that we need to sample more closely than 5m in our next surveys. We have not attempted a close detailed correlation of elevation, as the LiDAR processing includes vegetation height, the likely cause of some of the elevation peaks.

DISCUSSION

Our reconnaissance study aimed to characterize both larger (>100 m) and smaller scale geologic features (10–100 m) that could affect selection of sites for hydrologic models within the unsaturated zone. Smaller scale features were characterized by analyses of DEM, LiDAR, magnetics, magnetic susceptibility and conductivity data.

High pass filtering of DEM and LiDAR gave us an initial view of smaller scale differences, including distinctive stair-steps in topography that we believe are related to the differential resistance of surface and near surface material to erosion. Regions of above average topography (red colors, Figs. 4(a)–(b)) likely represent more resistant alluvial fan channels and associated crevasse splay deposits. Although some high areas exhibit outcrops of erosion resistant

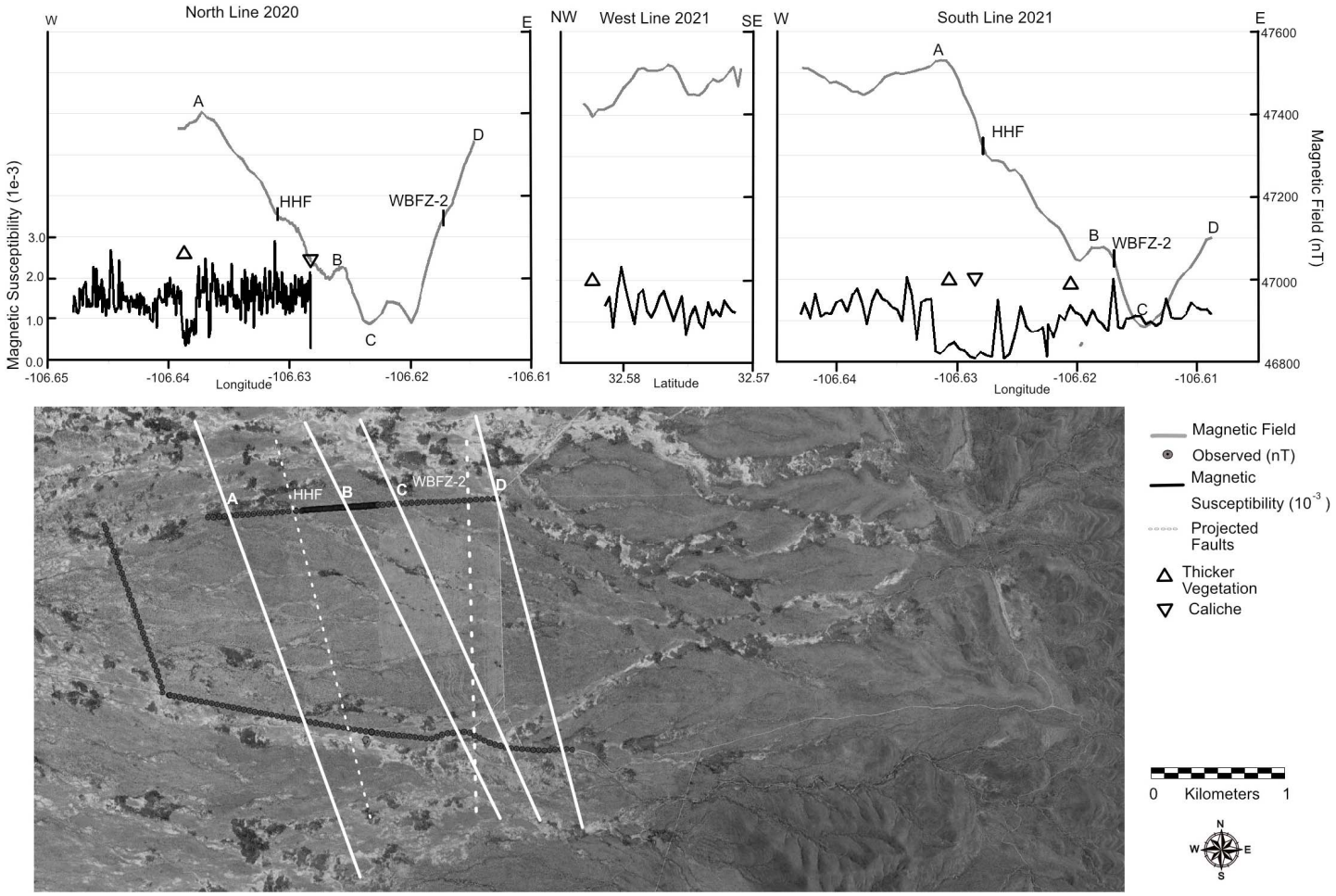

Figure 8 (top) Comparison of magnetic (upper lines) and magnetic susceptibility (lower lines) data collected at the Piedmont site. Letters refer to distinct features of the total magnetic field observed on both the north and south lines (see image at bottom). Inverted triangles indicate surface outcrops of pedogenic carbonates. Triangles indicate densely vegetated regions. Thick vertical lines indicate where the HHF and WBFZ-2 are inferred to cross the profiles. (bottom) Lines on the satellite image indicate the apparent trends of features A to D across the site.

pedogenic carbonates, we also find fine-grained sediments (some likely of eolian origin) in other regions of higher topography.

We hypothesize that the characteristic stair-step pattern is created by channels of different ages. The abundance of fine-grained sediment indicates the highs have been relatively stable surfaces in recent geologic time. Fig. 4(b) indicates that the rainfall infiltration experiment site (RE) is located on a stable surface of above average topography and may thus exhibit less variability than surrounding erosion dominated regions, making it a suitable location for the planned hydrologic experiments and borehole location.

Blue areas (lower than average topography) in Figs. 4(a)–(b) appear to be regions undergoing active erosion. Pebble-rich surface deposits are often seen at the surface in these regions, including the site of eddy flux covariance tower (FT, Fig. 4(b)). Researchers at the tower site have observed considerable erosion (both by up-slope wind and down-slope water) over the past 10 yr (based on photographs and video camera data collected during this time period), although the site is not located within an arroyo.

The magnetic highs and lows we observed (Fig. 8) are an order of magnitude greater than predicted from our simple geologic model (Fig. 6) based on Hawley and Kennedy's (2004) cross section that suggested extrusive Tertiary volcanics were buried beneath the site. In fact, we would require an intrusive unit beneath the site in order to obtain high enough magnetic susceptibility values to match the observed magnetic anomaly. The trends of features A through D (Fig. 8) are slightly oblique to the strike of extrapolated faults (HHM and WBFZ-2) and are more closely oriented to intrusive volcanic outcrop trends seen further to the southeast (Fig. 2). In our susceptibility surveys we have not found any rocks in the upstream outcrop or drainages with sufficient magnetite content to produce these anomalies. We expect to identify specific fault and intrusive body locations with ongoing additional gravity and seismic surveys. We can also be reasonably certain faults and intrusives affecting fluid flow are not passing through the areas

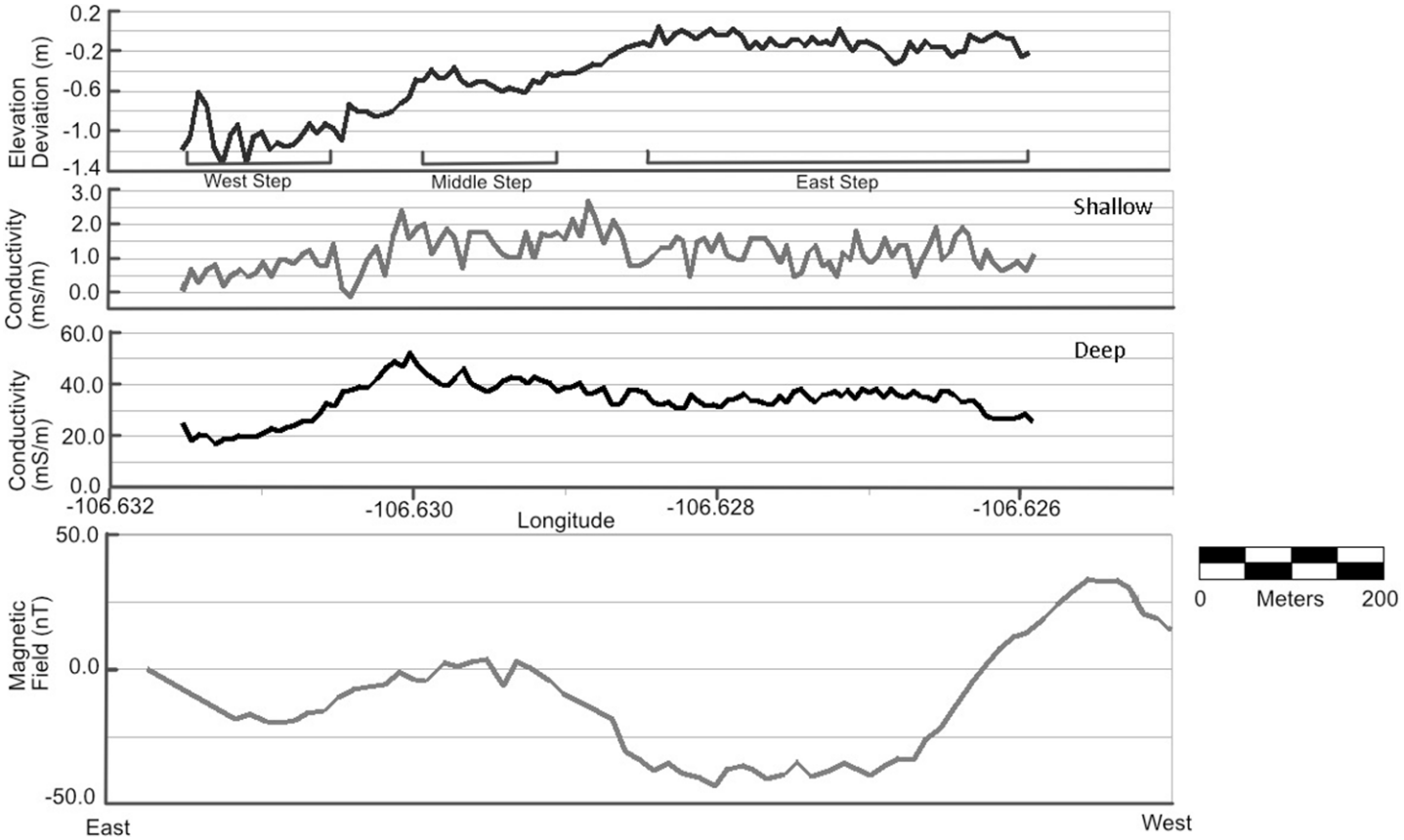

Figure 9 Ground conductivity values (middle lines) estimated from EM-31 measurements using the deconvolution method of McNeill (1980). The estimated shallow conductivity is the top conductivity plot and the estimated deep conductivity is the bottom conductivity plot. Elevation deviation as obtained from the LiDAR data is the topmost plot and the bottommost plot is the detrended magnetic field obtained from measurements collected ~75 m north of the conductivity measurements (see Fig. 7).

of consistent topography and low magnetic gradient needed for the siting of CZ experiments.

It is logical for two of the magnetic susceptibility lows (Fig. 8) to correlate with pedogenic carbonates, as these correspond to fan channels with a significant input of Paleozoic limestone, cemented by carbonates with low susceptibility. The other low-susceptibility regions are heavily vegetated, indicating shallow water availability, and might also be controlled by the pedogenic carbonates. Sand originating from fluvial channels of the ancestral Rio Grande found within the deepest part of the Jornada basin is blown by prevailing west and southwest winds across the Piedmont site. If these fluvial sand deposits are similar to deposits found in the El Paso area, they can reach 10% magnetite by weight (Sellepack, 2003). We expect that differences in topography and vegetation across the Piedmont site would lead to preferential grain size sorting and deposition of the wind-blown sand, with either coarser, heavier sands having higher magnetic signatures, or the magnetite being less likely to be picked up from finer-grained sands. The overall low observed susceptibility readings indicate that use of time domain electromagnetic (TDEM) moisture probes for the CZ site will not be affected by anomalous susceptibility.

In this desert region, shallow conductivity estimates in the range of 1 mS/m generally correspond to pedogenic carbonates and 2 mS/m to medium grained silicate sands with 1-2% volumetric moisture contents. The erosionally resistant surfaces seen in elevation maps correspond to the carbonates, while the more erodible transitions appear to be medium to fine sands. The low conductivities indicate ground penetrating radar will have good penetration depth and resolution, while permitting its use in mapping depth to the first pedogenic carbonate layer, which will strongly scatter the radar waves. The locally high carbonate content also points to a need for local calibration of each TDEM moisture probe.

At a larger scale, the presence of fault zones, intrusions, and the variation of bedrock topography likely play an important role in the hydrogeology of the Piedmont CZ. The deep conductivity estimate shows a strong lateral gradient that suggests a lateral water flow barrier in the vicinity of longitude −106.6305 (Fig. 9), a dramatic change in mineralogy or grain size, or the surface carbonate acting as an evaporation barrier. Previous studies within west

Texas (*e.g.,* Budhathoki *et al.*, 2018) have shown the important role fracturing within the hanging walls of normal faults plays in enhancing their permeability, allowing infiltration of surface water as well as upwelling of deep groundwater.

Both the DEM and magnetic data indicate that the HHF and WBFZ-2 likely extend across the Piedmont site, however magnetic data suggest other variations in basement structure must exist. The magnetic anomalies we observed are much larger than originally predicted from the inclusion of the solely extrusive volcanics across two fault zones (compare Fig. 6 to Fig. 8). As a consequence of the magnetic and conductivity anomalies, we have planned to extend our seismic and gravity surveys to cross anomaly D (Fig. 8) to assess water level changes across this feature.

Although topographic highs appear to have been relatively stable in recent time (over 0.7 m of fine grained material observed in preliminary test pit), the sides of a number of deeper arroyos show alternation of pebble layers, pedogenic carbonates and fine-grained material. This suggests there are changes in surface equilibrium over longer time scales. Whether these shifts in equilibrium are due to changes in climate or tectonics is an important question for future work.

Maciejewski and Miller (1998) observed several igneous intrusions that appear to act as barriers to water flow, as well as bedrock channels that enhanced water flow at the NASA site. We expect that similar structures likely exist at the Piedmont site. The total magnetic field (Fig. 5) at the Piedmont site is higher than at the NASA site. This requires that even more igneous rocks must be present in the Tertiary-Cretaceous (T-K) basement at the Piedmont site (Fig. 5). Ongoing seismic and gravity studies at the Piedmont site will help to better constrain the bedrock structure and its composition.

CONCLUSIONS

Although we have presented our study in a more traditional summary of data, methods and results format, the chronological order of our analyses was important to planning each step of the geophysical reconnaissance we conducted. The background studies of DEM, LiDAR and regional gravity/magnetics before going to site led us to focus on making detailed observations within specific regions of interest in our initial site visit, and to quickly exclude non-uniform sites from further consideration for the CZ facility. The background studies and site visit also helped us to identify the places where we needed to collect conductivity, magnetic and magnetic susceptibility data to verify compatible conditions. The complete reconnaissance process allowed us to identify regions affected by erosion to different degrees. This led to siting shallow coring profiles, and modifying the extent of seismic and gravity surveys. We also identified regions of near surface inhomogeneity (*e.g.,* near eddy flux covariance tower) that require additional geophysical study.

While we expected our reconnaissance would help us to identify where faults cut across the Piedmont site, the magnetic surveys indicate the bedrock structure was more complicated. An unexpected and unexplained linkage between the bedrock structure, shallow conductivity, and vegetation distribution led us to initiate additional geophysical studies.

The success of our reconnaissance work over three field days serves as a blueprint for preliminary characterization at other dryland CZ sites. We believe similar reconnaissance work could greatly assist in the siting of experiments at CZ sites in other regions.

References

Browning, D.M., Anderson, J.P., and Peters, D.C., 2011, Patterns in reproductive phenology for dryland grasses and shrubs from 1993 to 2010 in the Chihuahuan Desert, *in* Proceedings of the 96th Ecological Society of America Annual Meeting, COS 2-7.

Budhathoki, P., Doser, D.I., Thapalia, A., Langford, R.P., and Avila, V.M., 2018, Geological and geophysical studies of the structure and stratigraphy of the northwestern Hueco Bolson aquifer, El Paso, Texas: Geosphere, **14**, 731–784.

Eswaran, H., Reich, P.F., Kimble, J.M., Beinroth, F.H., Padmanabhan, E., and Moncharoen, P., 2000, Global carbon stocks, *in* Global Climate Change and Pedogenic Carbonates, Lal, R., Kimble, J.M., Eswaran, H., and Stewart, B.A. (eds.), Lewis Publishers, Boca Raton, Florida, 15–25.

Flinchum, B.A., Holbrook, W.S., Rempe, D., Moon, S., Riebe, C.S., Carr, B.J., Hayes, J.L., St. Clair, J., and Peters, M.P., 2018, Critical zone structure under a granite ridge inferred from drilling and three-dimensional seismic refraction data: J. Geophys. Res: Earth Surface, **123**, 1317–1343.

Khatun, S., Doser, D.I., Imana, E.C., and Keller, G.R., 2007, Locating faults in the southern Mesilla Bolson, west Texas and southern New Mexico, using 3-D modeling of precision gravity data: J. Envir. and Engineer. Geophysics, **12**, 149–161.

Hawley, J.W., and Kennedy, J.F., 2004, Creation of a Digital Hydrogeologic Framework Model of the Mesilla Basin and Southern Jornada del Muerto Basin: New Mexico Water Resources Research Institute WRRI Technical Completion Report No. 332.

Maciejewski, T.J., 1996, Integrated geophysical interpretation of bedrock geology, San Andres Mountains, New Mexico: M.Sc. thesis, The University of Texas at El Paso, El Paso, Texas.

Maciejewski, T.J., and Miller, K.C., 1998, Geophysical interpretation of subsurface geology, pediment of the San Andres Mountains to the Jornada del Muerto Basin, New Mexico, *in* Las Cruces Country II, Mack, G.H., Austin, G.S., and Baker, J.M. (eds.), New Mexico Geological Society 49th Annual Fall Field Conference Guidebook, 101–106.

McNeill, J.D., 1980, Electromagnetic terrain conductivity measurement at low induction numbers: Geonics Technical Note, TN-6.

Monger, H.C., and Martinez-Rios, J.J., 2001, Inorganic carbon sequestration in grazing lands, *in* The Potential of U.S. Grazing Lands to Sequester Carbon and Mitigate the Greenhouse Effect, Follett, R.R., Kimble, J.M., and Lal, R. (eds.), Lewis Publishers, Boca Raton, Florida, 87–118.

Novitsky, C.G., Holbrook, W.S., Pasquet, S., Okaya, D., and Flinchum, B.A., 2018, Mapping inherited fractures in the critical zone using seismic anisotropy from circular systems: Geophysical Research Letters, **45**, 3126–3135.

Olyphant, J., Pelletier, J.D., and Johnson, R., 2016, Topographic correlations with soil and regolith thickness from shallow-seismic refraction constraints across upland

hillslopes in the Valles Caldera, New Mexico: Earth Surf. Process. Landforms, **41**, 1684–1696.

Prăvălie, R., 2016, Drylands extent and environmental issues: A global approach: Earth-Science Reviews, **161**, 259–278.

Sellepack, B.P., 2003, Stratigraphy of the Pliocene-Pleistocene Camp Rice Formation in the Hueco and Mesilla Bolsons: M.Sc. thesis, The University of Texas at El Paso, El Paso, Texas.

Serna-Perez, A., Monger, H.C., Herrick, J.E., and Murray, L., 2006, Carbon dioxide emissions from exhumed petrocalcic horizons: Soil Science Society of America Journal, **70**, 795–805.

St. Clair, J., Moon, S., Holbrook, W.S., Perron, J.T., Riebe, C.S., Martel, S.J., Carr, B., Harman, C., Singha, K., and Richter, D. deB. 2015, Geophysical imaging reveals topographic stress control of bedrock weathering: Science, **350**(6260) 534–538.

United Nations Convention to Combat Desertification (UNCCD), 2000, Fact Sheet 2: The Causes of Desertification. United Nations Secretariat of the Convention to Combat Desertification, https://catalogue.unccd.int/935_factsheets-eng.pdf, last accessed March 17, 2021.

United States Geological Survey, 2021, TNM Download (V2.0), apps.nationalmap.gov/downloader/#/productSearch, last accessed March 31, 2021.

Zamanian, K., Pustovoytov, K., and Kuzyakov, Y., 2016, Pedogenic carbonates: Forms and formation processes: Earth-Science Reviews, **157**, 1–17.

Acknowledgments

We thank C. Montana for assistance with accessing the PACES gravity and magnetic database and G. Kaip for the maintenance and calibration of geophysical equipment used in this study. C. Tweedie shared important information regarding observations of erosion at the eddy flux tower site. L. Ma and M. Engle let us watch them dig the first soil test pit at the site. L. Baker assisted in collecting the magnetic susceptibility data on day two of the project. We thank JER personnel for granting permission to conduct our geophysical surveys. The Jornada Experimental Range (JER) is administered by the USDA-ARS and is supported by the National Science Foundation Long-Term Ecological Research Program and the USDA Long-Term Agroecosystem Research Network. Our study was supported by the National Science Foundation through NSF award #2012475